
Rotor Multi-Frequency Vibration Suppression Based on an Improved Differentiator

Xinyu Gao, Jian Xing and Changheng Yu

Beijing University of Chemical Technology, Beijing, 100029, China.

Jian Wang

Tianjin University, Tianjin, 300072, China.

Jianfei Yao

Beijing University of Chemical Technology, Beijing, 100029, China. E-mail: yaojf@mail.buct.edu.cn

(Received 10 August 2024; accepted 22 September 2024)

An approach of multi-frequency vibration suppression based on an improved differentiator is proposed to suppress the rotor vibration caused by unbalance and misalignment with an electromagnetic actuator (EA) in rotating machinery. The differentiator has a characteristic of acquiring a signal quickly and accurately. The accuracy and speed of vibration signal extraction are improved by optimizing the differentiator in the discrete PD algorithm. To begin with, a dynamic model of the rotor-bearing-EA system is established. The characteristics of rotor vibration caused by the rotor imbalance and misalignment are analyzed. Then, a notch filter, which can adjust the notch frequency according to the rotating speed in real time, is employed to extract the first and second harmonic components of the vibration signal. A control algorithm utilizing a modified differentiator is developed. The results of simulations and experiments show that the PD control employing the differentiator optimization algorithm can effectively suppress multi-frequency vibrations resulting from rotor imbalance and misalignment compared with the conventional PD control.

1. INTRODUCTION

Rotor vibration is a persistent issue in the realm of rotating machinery, exerting a significant influence on the operational stability of such machinery. The intricate and demanding working conditions, coupled with inherent rotor imbalances¹ and misalignments,² give rise to intricate vibrations during rotor operation. Failure to promptly and effectively mitigate these vibrations can exacerbate rotor vibration, potentially leading to accidents.

The active electromagnetic bearing possesses non-contact, friction-free, and non-lubricating characteristics,³ making it a suitable actuator for mitigating the vibration of rotors in rotating machinery.⁴ Electromagnetic bearings have found extensive applications in various industries such as the nuclear industry, life science industry, chemical industry, aerospace industry, and others.⁵ Zhu Changsheng et al.^{6,7} have developed a controller for an active electromagnetic bearing-rotor system, enabling active control of rotor vibration with consideration of multiple objectives. Wang Zhongbo et al.⁸ have addressed the issue of multi-frequency vibration in rotor systems through the utilization of current compensation. Guo et al.⁹ studied optimization algorithms for multiple rotors in unbalanced states to suppress rotor vibration and improve rotor vibration efficiency and speed. Deng et al.¹⁰ have employed constraint processing operators to facilitate decision-makers in achieving a balance between the diversity of necessary configurations and the performance of existing distribution controllers. This approach was utilized to address the electromagnetic bearings' multi-objective optimization configuration (EMAs MOOC) problem in the context of fault-tolerant control of magnetic bearing sys-

tems. Similarly, Yao Jianfei et al.^{11,12} have utilized a variable step size optimization strategy to determine the optimal current for the electromagnetic actuator. Furthermore, they implemented the current with multi-frequency components on the rotor to effectively suppress multi-frequency vibration through feedforward techniques.

In the realm of control algorithm design, Niu et al.¹³ have posited that incorporating the active noise control model (filtered-x least mean square, FxLMS) proves advantageous for addressing the time-dependent structure of vibration control. The efficacy of the FxLMS function is augmented through adjustment by the "bang-bang" controller. Zhou et al.¹⁴ have introduced the adaptive improved LMS algorithm with phase correction (C-LMS) algorithm, which effectively mitigates self-excited vibration across a broad frequency spectrum. The algorithm's robustness underscores its potential for application in magnetic suspension systems (EMS). Lin et al.¹⁵ have devised a novel vibration control approach. Saldanha et al.¹⁶ have introduced a control design approach that allows for the simultaneous manipulation of poles and zeros in a linear time invariant system, showcasing its effectiveness in mitigating vibrations in spring mass damper systems. Conversely, Zheng et al.¹⁷ have employed a feedforward control algorithm to address rotor vibration. Despite this, they encountered challenges in terms of disturbance resistance and control stability. In contrast, Yao et al.¹⁸ have utilized a PD feedback control algorithm that exhibited remarkable stability; however, it suffered from limited control accuracy when subjected to harsh working conditions and full frequency random noise. Bao et al.¹⁹ have improved the iterative learning control algorithm and ap-

plied it to reduce the rotor vibration generated by the rotor under complex working conditions, so as to improve the original control effect. Gao et al.²⁰ have proposed a nonlinear optimization algorithm based on the immersion invariant method to suppress the single frequency and multiple frequency vibration signals generated in the process of rotor operation. In summary, the collective findings of these studies shed light on the various control methods and their respective strengths and limitations. The overall algorithm needs further improvement and optimization, especially in differential signal recognition improvement.

The utilization of derivatives has proven to be highly advantageous in the field of control. Stanić et al.²¹ have devised an improved near-linear phase IIR full-band differential to address the prevalent issue of diminishing spectrum content with increasing frequency. Zhang et al.²² have conducted an analysis and validation of the convergence of tracking derivatives for auto-rejection control. Seeber et al.²³ have examined the worst-case error range of the super-twist differential in the presence of measurement noise. Recently, high-gain observers have emerged as a remarkably efficacious instrument for observation systems.^{24,25} The expeditious resolution of real-time signals has emerged as an imperative factor to be considered. Within these signals, the predominant techniques employed involve the establishment of a differentiating device. This device serves the purpose of swiftly extracting and differentiating the vibration signal, thereby enabling it to significantly contribute to the control field in terms of speed measurement.^{26,27} In the context of constructing a linear observer, its primary objective is to approximate the original signal into an ideal transfer function within its frequency domain. Currently, there is a lack of experimental research on the application of the differential algorithm in rotor vibration suppression. However, the differential algorithm exhibits significant advantages in signal extraction and optimization, which are highly beneficial for advancing the field of rotor vibration suppression. Consequently, this study enhances the existing differential algorithm by incorporating knowledge of power frequency vibration and devises an improved version to optimize rotor vibration suppression.

A fast-differentiating device is designed in accordance with the traditional PD control algorithm in the work. The vibration signal is subjected to processing through a low-pass filter and discretized using either differential or high-precision numerical iteration methods. The derivative of the signal extraction is employed to achieve control without the need for speed measurement. The electromagnetic actuator (EA) is utilized as the actuator, and a PD control algorithm is developed based on the enhanced differentiating device. This algorithm effectively suppresses the rotor multi-frequency vibrations resulting from rotor unbalanced and misaligned in rotating machinery.

2. METHODOLOGY

2.1. Model of Rotor-Bearing-EA System

Rotor-bearing-EA system is shown in Fig. 1. The equation of the rotor-bearing-EA system is shown in Eq. (1):

$$\mathbf{M}\ddot{\mathbf{Z}} + \mathbf{C}\dot{\mathbf{Z}} + \mathbf{K}\mathbf{Z} = \mathbf{F}_1 + \mathbf{F}_2; \quad (1)$$

where \mathbf{M} is the mass matrix, \mathbf{C} is the damping matrix, \mathbf{K} is the stiffness matrix, and \mathbf{Z} is displacement vector respectively.

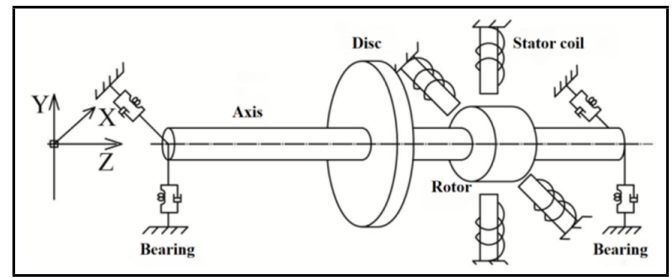


Figure 1. Rotor-bearing-EA system.

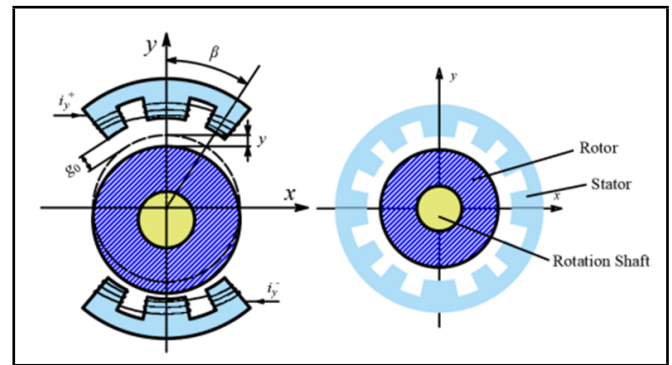


Figure 2. Schematic diagram of magnetic bearing structure (y direction).

The vector \mathbf{F}_1 contains unbalanced excitation and maladjusted excitation, and \mathbf{F}_2 is the electromagnetic control force generated by EA in the system.

A radial electromagnetic bearing is applied as electromagnetic actuator. The magnetic pole is an E-shaped 12 pole unequal magnetic pole structure, as shown in Fig. 2.

The magnetic bearing is composed of stator, rotor and rotating shaft. The 12 magnetic poles are divided into four regions, and each region is composed of a main magnetic pole and two sub magnetic poles. Angle between two magnetic poles, β is 33° , and the clearance distance between the rotor and the shaft under static state is g_0 , simultaneously considering vacuum magnetic permeability μ_0 . After the magnetic bearing is energized, the magnetic force generated by it is shown in Eq. (2):¹⁸

$$F_{\text{mag}}^y = k_a \left[\left(\frac{i_y^+}{g_0 + y} \right)^2 - \left(\frac{i_y^-}{g_0 - y} \right)^2 \right]; \quad (2)$$

where k_a is the characteristic coefficient of AMA magnetic pole group, $k_a = 49\mu_0 A_0 N^2 (1 + \cos \beta) / 128$, N is the number of turns of the electromagnetic coil, A_0 is the maximum magnetic pole area, i_y^\pm is the current generated inside the coil, g_0 is the clearance between the rotor and stator of the motor, which has been marked in Fig. 2.

The electromagnetic force is a binary quadratic nonlinear function of rotor displacement and coil current in Eq. (2). Equation (3) is obtained by the first-order Taylor expansion of Eq. (2) at the operating point $(0, 0)$ to reduce the influence of electromagnetic force nonlinearity:

$$F_{\text{mag}}^y = -k_s y + k_i i_{cy}; \quad (3)$$

where k_s is displacement stiffness, $k_s = 4k_a i_0^2 / g_0^3$, and k_i is current stiffness, $k_i = 4k_a i_0 / g_0^2$, g_0 is the static air gap.

It is assumed that the air gap g_0 in the x and y directions is uniform, and the magnetic pole area A_0 is the same. Moreover,

the influence of magnetic leakage and magnetic field coupling is not considered. The current stiffness and displacement stiffness in the x and y directions can be equal. Equation (4) can be obtained as:

$$\mathbf{F}_{\text{mag}}^e = \begin{bmatrix} F_{\text{mag}}^x \\ F_{\text{mag}}^y \end{bmatrix} = -k_s \begin{bmatrix} x \\ y \end{bmatrix} + k_i \begin{bmatrix} i_{cx} \\ i_{cy} \end{bmatrix} = -k_s \mathbf{z}_a + k_i \mathbf{i}_c. \quad (4)$$

F_{mag} in the local coordinate system is used as the control force, which is transferred to the global coordinate system. The expression of the control force \mathbf{F}_2 can be obtained as:

$$\mathbf{F}_2 = \mathbf{T}_c^T [-k_s \mathbf{T}_c \mathbf{Z} + k_i \mathbf{i}_c]; \quad (5)$$

where \mathbf{T}_c is the conversion matrix, \mathbf{i}_c is the control current, k_s is the displacement stiffness, and k_i is the current stiffness, respectively.

The interference force and control force are integrating into Eq. (1) as:

$$\mathbf{M}\ddot{\mathbf{Z}} + \mathbf{C}\dot{\mathbf{Z}} + \{\mathbf{K} + k_s \mathbf{T}_c^T \mathbf{T}_c\} \mathbf{Z} = \mathbf{F}_1 + k_i \mathbf{T}_c^T \mathbf{i}_c; \quad (6)$$

where \mathbf{T}_c is the electromagnetic force matrix.

2.2. State Space Equation

The state space vector is defined as:

$$\mathbf{q} = [\mathbf{Z} \ \dot{\mathbf{Z}}]^T, \quad \dot{\mathbf{q}} = [\dot{\mathbf{Z}} \ \ddot{\mathbf{Z}}]^T. \quad (7)$$

The inverse solution of Eq. (6) is transformed into a first-order differential equation, as shown in Eq. (8):

$$\begin{bmatrix} \dot{\mathbf{Z}} \\ \ddot{\mathbf{Z}} \end{bmatrix} = \begin{bmatrix} \mathbf{0} & \mathbf{I} \\ -\mathbf{M}^{-1} \mathbf{K}_1 & -\mathbf{M}^{-1} \mathbf{C} \end{bmatrix} \begin{bmatrix} \mathbf{Z} \\ \dot{\mathbf{Z}} \end{bmatrix} + \begin{bmatrix} \mathbf{0} \\ \mathbf{M}^{-1} \end{bmatrix} k_i \mathbf{T}_c^T \mathbf{i}_c + \begin{bmatrix} \mathbf{0} \\ \mathbf{M}^{-1} \end{bmatrix} \mathbf{F}_1. \quad (8)$$

The system matrix, electromagnetic force matrix and interference force matrix in Eq. (7) are substituted into the state space vector from Eq. (6) as:

$$\dot{\mathbf{q}} = \mathbf{A}_s \mathbf{q} + \mathbf{B}_{sa} \mathbf{i}_c + \mathbf{B}_{su} \mathbf{F}_1; \quad (9)$$

where \mathbf{A}_s is the system matrix, \mathbf{B}_{sa} and \mathbf{B}_{su} are the input matrices of AMA current and interference force respectively.

Equation (9) is the governing equation of the rotor-bearing-AMA system. The differential equation can be solved by ode series solver (e.g. variable step ode45) in simulation.

2.3. Derivation Theory

Khalil²⁹ has designed a linear high-gain derivative or a linear derivative tracking derivative (high-speed derivative). Main forms of high gain differentiating device are as follows:

$$\dot{\bar{y}} = A\dot{y} + B(v(t) - c\bar{y}); \quad (10)$$

where $y = [y_1 \ \dots \ y_{n-1} \ y_n]^T$, $A = [a_1/\varepsilon \ a_2/\varepsilon^2 \ \dots \ a_n/\varepsilon^n]^T$ (ε is a positive parameter to

be specified.), $B = \begin{bmatrix} 0 & 1 & 0 & \dots & 0 \\ 0 & 0 & 1 & \dots & 0 \\ \vdots & \vdots & \vdots & \ddots & \vdots \\ 0 & 0 & 0 & \dots & 1 \\ 0 & 0 & 0 & \dots & 0 \end{bmatrix}$, $c = [1 \ 0 \ \dots \ 0]$,

a_1, \dots, a_n are constants and the real part of the characteristic root that needs to meet the characteristic equation $s^n + a_1 s^{n-1} + \dots + a_{n-1} s + a_n = 0$ is negative.

The fast differential in the whole process is as shown in Eq. (11):

$$\begin{cases} \dot{x}_1 = x_2; \\ \dot{x}_2 = R^2 \left\{ -a_0 [x_1 - v(t)] - a_1 [x_1 - v(t)]^{\frac{m}{n}} - b_0 \frac{x_2}{R} - b_1 \left(\frac{x_2}{R} \right)^{\frac{m}{n}} \right\}; \\ y = x_2(t); \end{cases} \quad (11)$$

where R is the adjustment parameter of the differential, a_0 and b_0 are linear adjustment parameters, a_1 and b_1 are nonlinear adjustment parameters, m and n are odd numbers greater than 0, and $m < n$. The first derivative $\dot{v}(t)$ of the tracking signal $v(t)$ of the system output $y = x_2(t)$. When $a_1 = b_1 = 0$, the linearity of the line differentiator plays a leading role. The improved differentiator is shown in Eq. (12):

$$\begin{cases} \dot{x}_1 = x_2; \\ \dot{x}_2 = R^2 \left\{ -a_0 [x_1 - v(t)] - b_0 \frac{x_2}{R} \right\}; \\ y = x_2(t). \end{cases} \quad (12)$$

It is observed that each layer of the high gain differentiating device may experience a certain level of disturbance, as well as a peak value phenomenon. Specifically, when the gain approaches the values of infinity or infinitesimal, the transient output of the differentiating device tends to increase infinitely, while its impact on high order white noise is not readily apparent. The whole-process fast differential device offers certain enhancements to address these limitations. Moreover, the discretization of the differential device allows for direct analysis of vibration control.

3. CONTROLLER DESIGN

3.1. Control Law Design

The Proportional Integral Differential (PID) control algorithm, which is widely employed in general control systems, was initially utilized for the control of electromagnetic bearings. As an illustration, considering the displacement signal $y(t)$ with sampling number t in the y -direction, assuming the desired output is $y_d(t)$ and the system deviation is $error(t) = y_d(t) - y(t)$, the time-domain control law of the PID control algorithm can be expressed in Eq. (13):

$$u(t) = k_p \left[error(t) + \frac{1}{T_I} \int_0^t error(\tau) d\tau + \frac{T_D}{dt} d error(t) \right]; \quad (13)$$

where k_p is the proportional coefficient, T_I is the integral time constant, and T_D is the differential time constant.

Integral control is mainly used to eliminate overshoot or integral saturation caused by improper selection of system static error. PD control algorithm is adopted for active suppression of multiple frequency periodic vibration:

$$u(t) = k_p \left[error(t) + \frac{T_D}{dt} d error(t) \right]. \quad (14)$$

Let $T_d = k_p T_D$, it is obtained that:

$$u(t) = k_p \text{error}(t) - T_d \text{error}'(t). \quad (15)$$

Considering the vibration suppression of each discrete point, a small distance between discrete points can be approximately regarded as infinitely continuous. The discrete period is T_0 , the number of sampling signals is k , so the continuous time t can be expressed as kT_0 , and Eq. (16) can be obtained:

$$\begin{cases} t = kT_0, & (k = 0, 1, 2, \dots); \\ \frac{d \text{error}}{dt} = \frac{\text{error}(k) - \text{error}(k-1)}{T_0}; \end{cases} \quad (16)$$

where $\text{error}(k)$ and $\text{error}(k-1)$ are deviation signals measured at time k and $k-1$ respectively. The discrete expression of $u(k)$ is shown in Eq. (17)

$$u(k) = k_p \text{error}(k) + T_d \frac{\text{error}(k) - \text{error}(k-1)}{T_0}. \quad (17)$$

3.2. Improvement of Differential Device Design

The measured vibration signal is substituted into the fast-differentiating device. The vibration signal in the y -direction is taken as an example. Comprehensive Eq. (13), the introduced fast tracking control system is as follows:

$$\begin{cases} \dot{y}_1(k) = y_2(k); \\ \dot{y}_2(k) = R^2 \left\{ -a_0[y_1(k) - y(k)] - b_0 \frac{y_2(k)}{R} \right\}; \\ y = y_2(k). \end{cases} \quad (18)$$

where a_0 and b_0 are linear adjustment parameters, $y(k)$ is the amplitude of the rotor in the y -direction at time k , $y_1(k)$ is the process iteration parameter, $y_2(k)$ is the result iteration parameter. In the fast tracker system (PD&DA), the process parameter $y_1(k)$ is introduced, where $y_1(k)$ is the reciprocal of the system output result parameter $y_2(k)$. According to the theory of fast differentiators, the process parameter $y_1(k)$ and system input $y(k)$ are introduced into the differential equation formula solved by the system. By solving the differential equation, the result parameter $y(k)$ is obtained. The convergence of the differential will be proved as follows.

In the rotor vibration suppression system, $a_0, b_0 > 0$. The larger the adjustment parameter R of the differential design, the closer the output amplitude signal of the differentiator is to the actual vibration amplitude of the rotor under working conditions. Then for any input signal $y(k) \in [0, +B]$ ($0 < B < +\infty$). When the adjustment parameter R approaches infinity, Eq. (19) can be obtained as:

$$\lim_{R \rightarrow \infty} y(k) - y_1(k) = 0. \quad (19)$$

The fast differentiator (PD&DA) discusses the input signal $y(k)$ in two cases. One is when B is constant, the other is when B is infinite. The amplitude of rotor vibration is a constant, so we only consider the first case. The control output is written as:

$$\begin{cases} \frac{d(y_1(k) - c)}{dRk} = R^{-1}y_2(k); \\ \frac{d(R^{-1}y_2(k))}{dRk} = -a_0(y_1(k) - c) - b_0(R^{-1}y_2(k)). \end{cases} \quad (20)$$

Let $h = Rk$, $z_1(h) = y_1(k) - c$, $z_2(h) = R^{-1}y_2(k)$. At any sampling time node k_0 , there is as seen below:

$$\begin{aligned} \lim_{R \rightarrow \infty} \int_{k_0}^{k_0+K} |y_1(k) - c| dk &= \lim_{R \rightarrow \infty} \frac{\int_{Rk_0}^{Rk_0+RK} |z_1(Rk)| d(Rk)}{R} \\ &= \lim_{R \rightarrow \infty} \frac{\int_{Rk_0}^{Rk_0+RK} |z_1(h)| d(h)}{R}. \end{aligned} \quad (21)$$

1) When $\int_{Rk_0}^{Rk_0+RK} |z_1(h)| d(h) = \text{const}$, the left end of Eq. (21) is zero.

2) When $\int_{Rk_0}^{Rk_0+RK} |z_1(h)| d(h) \rightarrow \infty$, Eq. (22) can be obtained from Lobitar's law as:

$$\begin{aligned} \lim_{R \rightarrow \infty} \int_{k_0}^{k_0+K} |y_1(k) - c| dk &= \\ \lim_{R \rightarrow \infty} (|z_1(Rk_0 + RK)|(k_0 + K) - |z_1(Rk_0 + RK)|k_0). \end{aligned} \quad (22)$$

If $a_0, b_0 > 0$, then the differentiator system is tightly stable at point $(0, 0)$, which satisfies. Equation (22) can be simplified as:

$$\lim_{R \rightarrow \infty} \int_{k_0}^{k_0+K} |y_1(k) - c| dk = 0. \quad (23)$$

When $y(k) = \text{const}$, $R \rightarrow +\infty$, $y_1(k)$ converges weakly to B , and $y_2(k)$ tracks the differential signal of $y(k)$. Thus, Eq. (19) holds and the convergence of PD-DA can be demonstrated.

Finally, $y_2(k)$ is the new vibration signal processed by the differential:

$$\text{error}_2(k) = y_2(k). \quad (24)$$

Take it back to Eq. (17):

$$u(k) = k_p \text{error}(k) + T_d \frac{\text{error}_2(k) - \text{error}_2(k-1)}{T_0}. \quad (25)$$

The enhanced differential iteration can be discretized using the difference and high-precision numerical iteration method, employing the improved linear differential. Consequently, the differential demonstrates rapid convergence when the system deviates from the equilibrium point. However, as the system gradually approaches the equilibrium point, the convergence speed gradually diminishes. The acceleration during the initial phase holds significant importance in effectively mitigating vibrations and facilitating prompt restoration of the rotor system to its equilibrium position. In terms of reducing rotor amplitude, the ultimate stage of control primarily relies on the implementation of proportional-derivative (PD) control.

The parameters k_p and T_d in the derived algorithm in Eq. (25) are analyzed by an empirical patching method. In this work, the gain coefficients of the sensor and the power amplifier are set as W_c and W_g , respectively. It can be obtained by increasing the sensor signal gain to the original deviation signal. Comprehensively considering the power amplifier gain, Eq. (26) can be obtained as:

$$i_a(k) = W_g u(k) = -W_g W_c k_p z(k) - W_g W_c T_d \dot{z}(k). \quad (26)$$

The displacement stiffness coefficient W_s and current stiffness coefficient W_i of electromagnetic actuator shall be considered during the application of electromagnetic force. Take the horizontal force as an example:

$$F_x(k) = W_s x + W_i i_x. \quad (27)$$

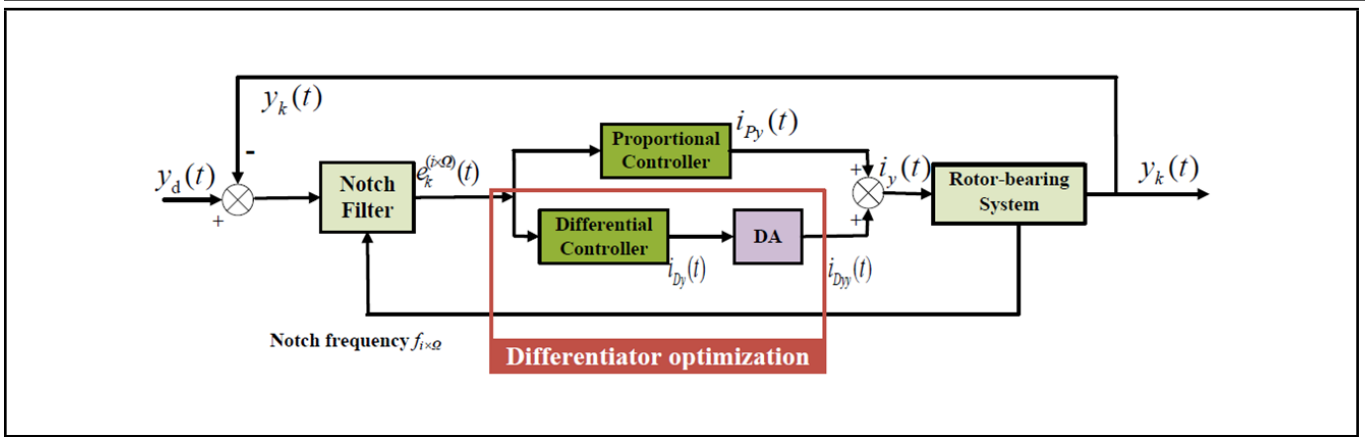


Figure 3. Block diagram of control system.

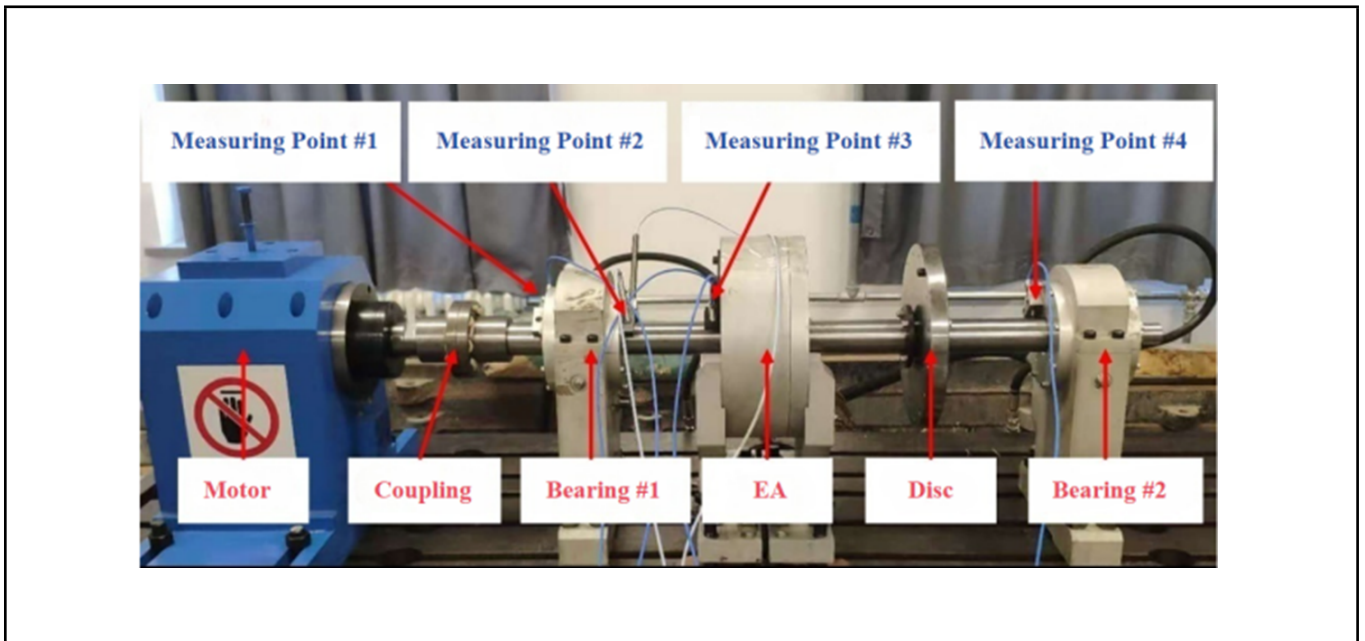


Figure 4. Test rig of Rotor-Bearing-EA System.

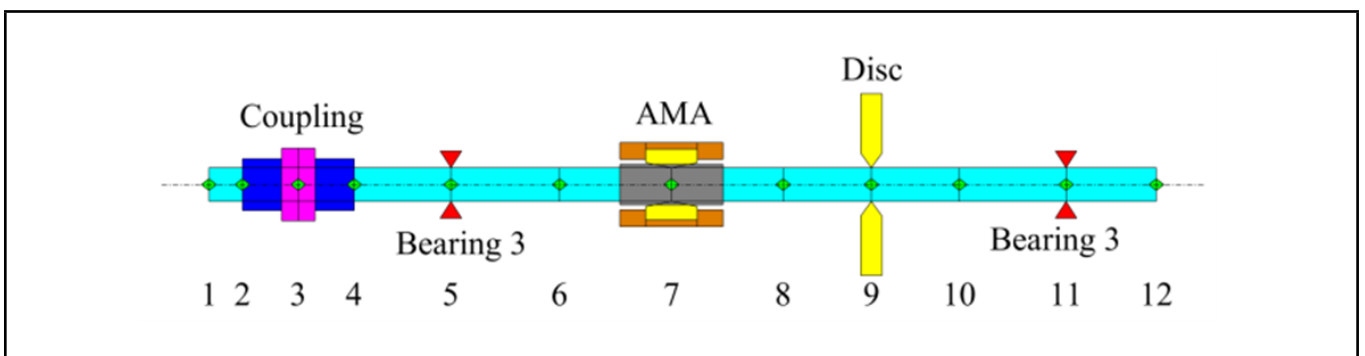


Figure 5. Diagram of model.

The discretization of Eq. (27) in the horizontal direction yields:

$$\begin{aligned}
 F_x(k) &= W_s z(k) + W_i (-W_g W_c k_p z(k) - W_g W_c T_d \dot{z}(k)) \\
 &= W_s z(k) - W_i W_g W_c k_p z(k) + W_i W_g W_c T_d \dot{z}(k).
 \end{aligned}
 \tag{28}$$

It can be seen that the rigidity provided by the electromagnetic actuator is negative for the whole system, i.e., $W_s < W_i W_g W_c k_p$, so the controller is required to provide the posi-

tive rigidity k_p in the subsequent control process.

When k_p is selected and determined, it is positioned according to the empirical trial method mentioned above. The dichotomous method can be used to find the reasonable integral constant.

Figure 3 shows the control flow chart of the improved differentiator algorithm system. An improved fast differentiator is added to the differential part of the PD control algorithm to enhance the control effect of the entire system on vibration.

Table 1. Parameters of the test rig.

	Parameters	Values
AMA	Magnetic pole area (A)	10^{-4} m ²
	Turns of large coils (N)	100
	Turns of small coils	75
	Rotor diameter	125 mm
	Stator diameter	126.2 mm
	Air gap(g_0)	0.6 mm
Rotor	Length of shaft	1 m
	Outer diameter	50 mm
	Thickness of disc	25 mm
	Diameter of disc	270 mm
Bearings	Number of pads	5
	Preloading	0.3
	Clearance	0.05 mm
Coupling	Half coupling length	65 mm

3.3. Filter Design

The notch filter is a second-order ($N = M = 2$) infinite impulse response digital filter, and its recursive equation is shown in Eq. (29)

$$y_f(n) = - \sum_{k=1}^M a_k y_f(n-k) + \sum_{k=0}^N b_k y(n-k); \quad (29)$$

where a_k and b_k are polynomial coefficients, $y_f(n)$ is the filtered processing value of the displacement signal $y(n)$ at time n .

Considering the need of multi-speed control and accurate target suppression, the polynomial coefficients are determined by a real-time table look-up of real-time speed and notch bandwidth.

4. SIMULATION

4.1. Description and Modeling of Test Rig

The test rig of a rotor bearing EA system is shown in Fig. 4. There are motor, coupling, bearing #1, EA, disc and bearing #2. Six displacement sensors are installed on the test bench. After the power supply is connected, the motor drives the shaft to rotate. The sampling rate f_s of the control system is 10.24 kHz. The other relevant parameters of the test rig are shown in Table 1.

The finite element model of the rotor system is shown in Fig. 5. The model includes coupling, shaft, bearing, EA and disc. The shaft is divided into 11 shaft segments and 12 nodes are marked. The coupling is located at nodes 2, 3 and 4. The two bearings are respectively located at nodes 5 and 11. The electromagnetic actuator (EA) and the disc are respectively located at nodes 7 and 9.

4.2. Simulation of Control Effect

In the simulation process, the sampling frequency of PD control system f_s is $f_s = 10$ kHz, rotor rotational frequency f is $f = 100$ Hz, proportional gain $K_p = 4 \times 10^7$, differential gain $K_D = 10$, and the control part of the differential converter takes $R = 1700$, $a_0 = b_0 = 4$ (R , a_0 and b_0 are the adjustment parameters of the high-speed differentiator) in simulation. The axis locus at the node of electromagnetic actuator before and after PD control are shown in Fig. 5. It becomes evident that the PD control algorithm with the improved differentiator has better effect compared with the traditional PD control in the case of the same PD control parameters.

Table 2. Parameters of algorithm.

Parameters	K_{p_x}	K_{p_y}	K_{D_x}	K_{D_y}	R	a_0	b_0
PD	10^4	-2.5×10^4	6	8	/	/	/
PD&DA	10^4	-2.5×10^4	6	8	1400	5	5

The alterations of rotor amplitude in each direction are presented in Fig. 6. As shown in Figs. 6(a) and (b), the blue line and red line are the rotor axis trajectory before and after control. It can be inferred that the traditional PD control exhibits vibration suppression effects of 45.67% and 45.74%, respectively. Through the comparison of vibration suppression effect data, the control effect of the differential improvement is increased by more than 30% based on the original algorithm.

Simulation images of the horizontal and vertical rotor amplitudes are displayed in Fig. 7, clearly demonstrating that the control effect of the improved differentiator algorithm significantly surpasses that of the PD algorithm.

Additionally, the first and second harmonic components experience notable suppression, as depicted in Fig. 8. The enhanced differentiator algorithm (PD&DA) demonstrates a substantial advancement in amplitude suppression of the first harmonic component.

In Figs. 9 and 10, the simulation is carried out under the condition of multiple speeds to observe whether the improved algorithm of the fast differentiator still has a good effect on vibration suppression.

In Fig. 11, the rotor's vibration amplitude increases from 25 μ m to 66 μ m as the rotational speed ranges from 1200 r/min to 2200 r/min. As the speed increases, the rate of amplitude growth also markedly accelerates. Gray bars represent the original vibration amplitude, while blue and green ones indicate the PD control and the improved fast differentiator control, respectively. Both demonstrate an inhibitory effect on amplitude across various rotational speeds, with the fast differentiator algorithm consistently outperforming the PD algorithm. As rotational speeds increase, the effectiveness of both control methods diminishes (as depicted in Fig. 12). The red and blue lines in Fig. 12 represent the amplitude control suppression rates for PD&DA and PD across various rotational speeds. The PD control algorithm achieves an amplitude suppression rate ranging from 43.7% to 48.8% at varying speeds, while the PD&DA control algorithm's rate ranges from 75.1% to 81.2%. This verifies that PD&DA significantly outperforms the PD algorithm in suppressing amplitude at various rotational speeds.

5. EXPERIMENT

The active suppression of rotor vibration at multiple speeds is conducted to verify the effectiveness of the proposed algorithm compared to the conventional PD control algorithm on the test rig. Parameters of the controllers were selected by the trial and error method, as shown in Table 2.

During the experiment, when the control switch is turned on at the tenth second, as shown in Figs. 13–14(a) (b), it can be seen that the vibration amplitude of the rotor decreases significantly. The amplitude of rotor vibration in the y -direction at the measurement point #1 before and after the PD controller is obtained, as shown in the Figs. 13–14(a). The amplitude of rotor vibration in the y -direction at the measurement point #1 before and after the PD&DA controller is shown in the Figs. 13–14(b). At the same time, as shown in Figs. 13–14(c) (d), the

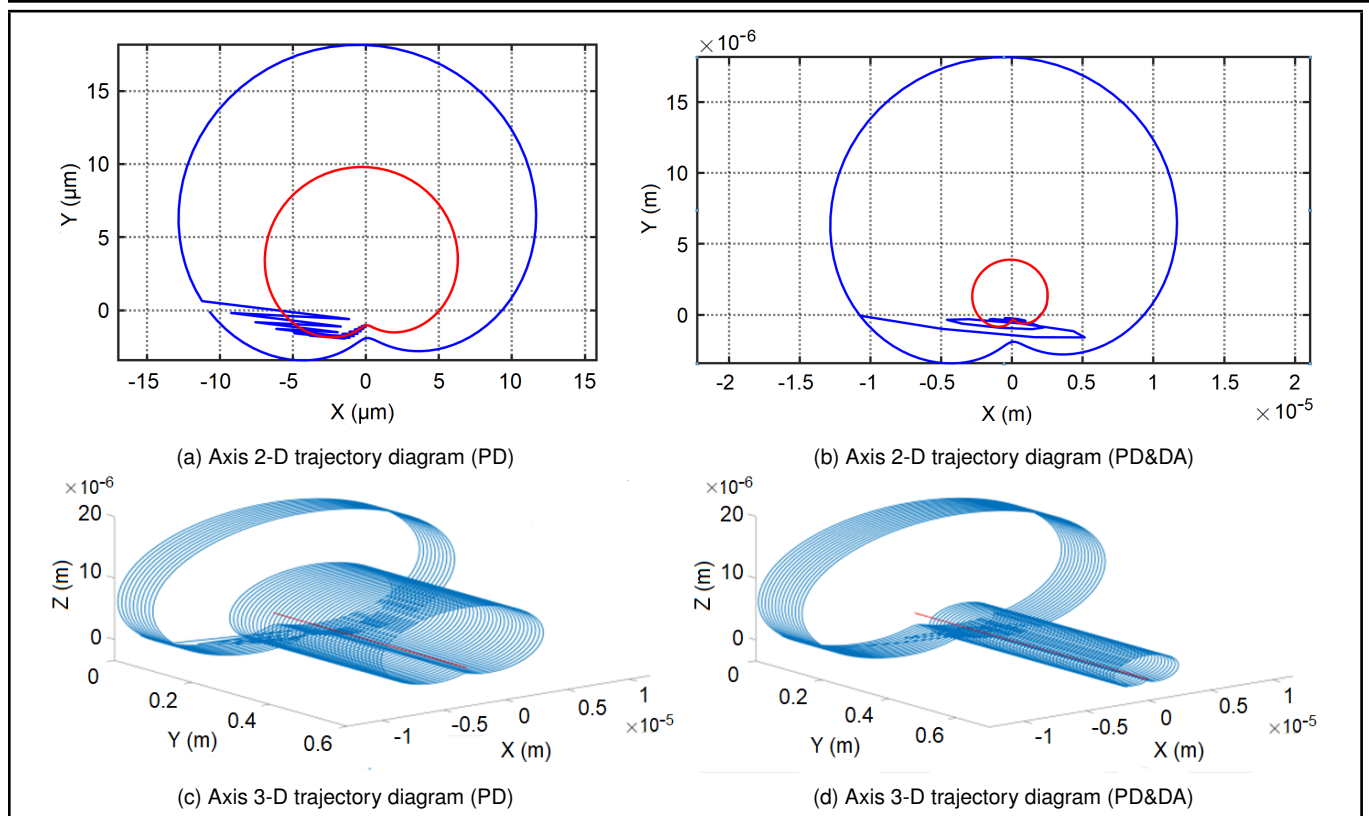


Figure 6. 2D and 3D trajectory diagram of electromagnetic actuator nodes.

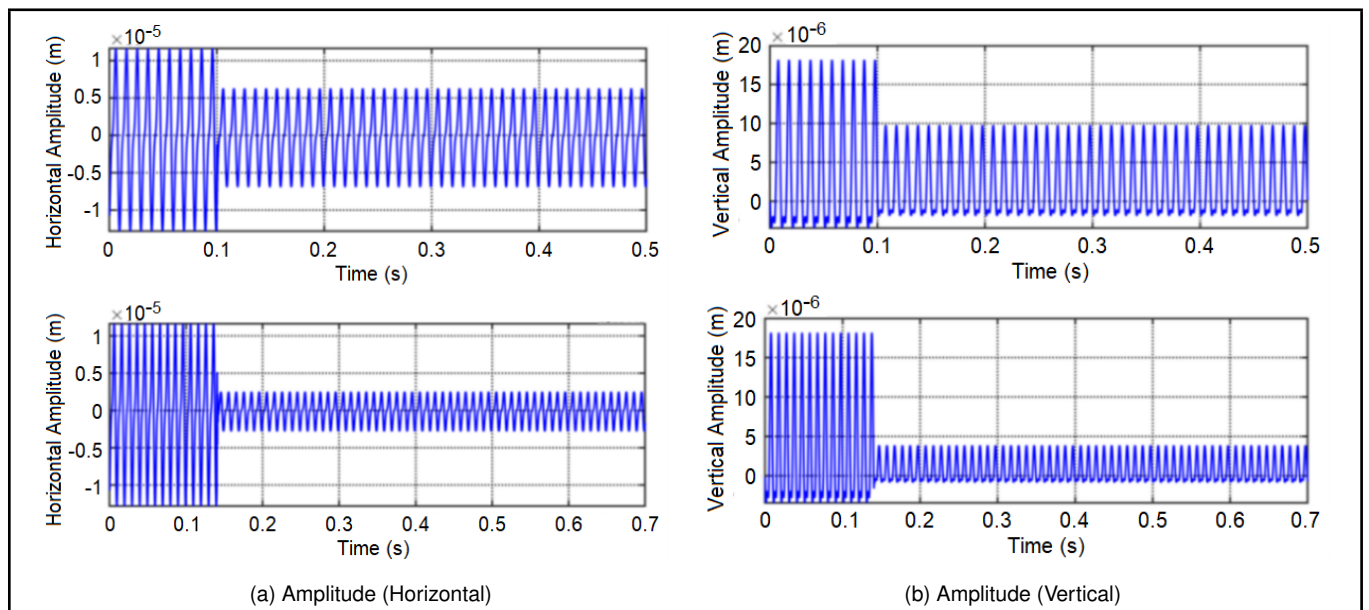


Figure 7. Rotor amplitude in X and Y directions at the nodes of electromagnetic actuators.

coil current of EA is applied in the 10th second. A comparative experimental approach was employed to enhance the visibility of the experimental effect. The experimental findings depicted in Figs. 13–14 substantiate the efficacy of the PD algorithm and differentiator optimization algorithm in mitigating rotor vibration, as observed from a temporal perspective.

Figure 15 shows the image of the axis trajectory of the 5th, 10th and 15th seconds under the control of the rotating speed at 1500 r/min, representing the image of the axis trajectory of the implementation at three times before, during and after the control, respectively. It is obvious that both algorithms play a role

in vibration suppression after being applied, and PD&DA has more advantages in control effect. However, in terms of the recognition of vibration signals and the effectiveness of control, the differentiator optimization algorithm exhibits a significantly superior performance compared to the PD control algorithm. For instance, when considering a rotational speed of 1350 r/min, the improved differentiator algorithm achieves an amplitude suppression rate of 43.27%, whereas the PD control algorithm only achieves 27.62% (see Fig. 13). Moreover, from the control effect, it is observed that the improved algorithm of the differentiator is applied to the rotor, and its vibration

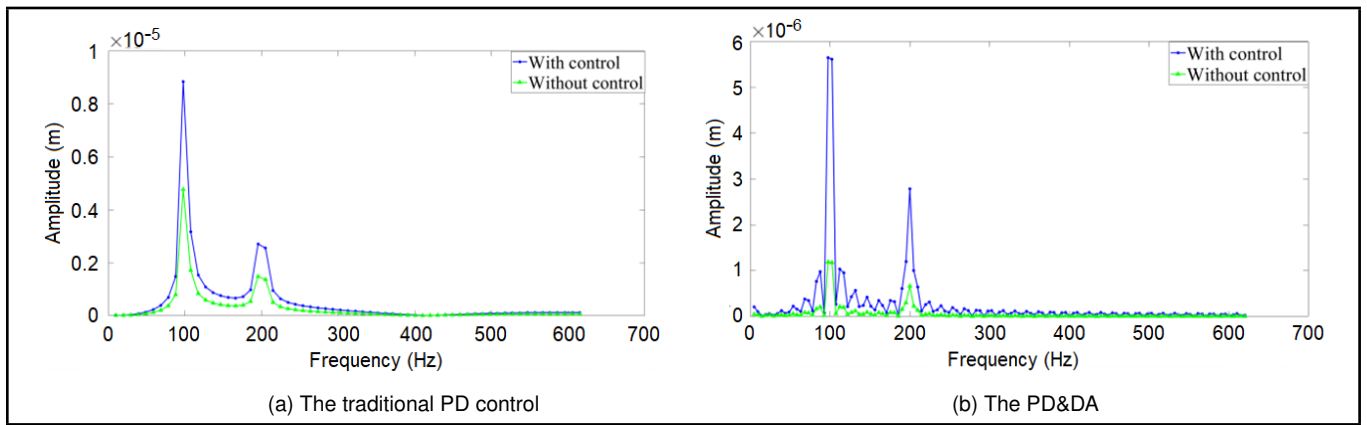


Figure 8. Spectrum diagram at the AMA nodes before and after control (*x*-direction).

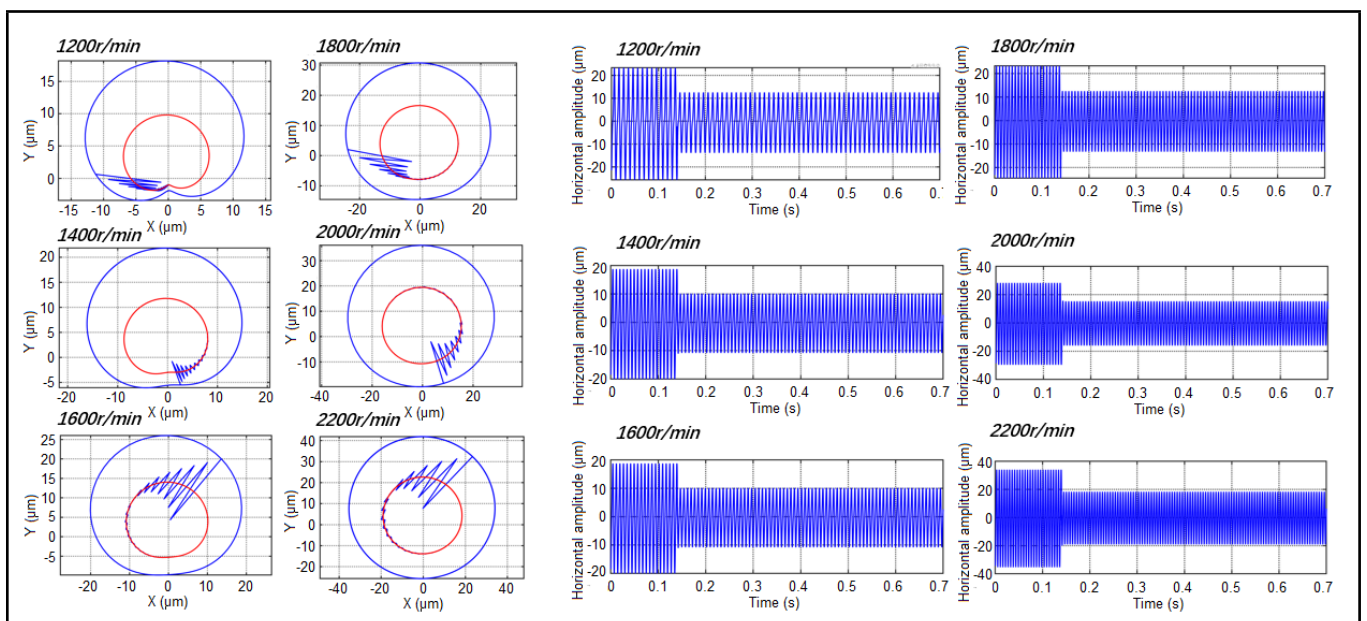


Figure 9. Diagram of axis trajectory and horizontal amplitude with PD control algorithm.

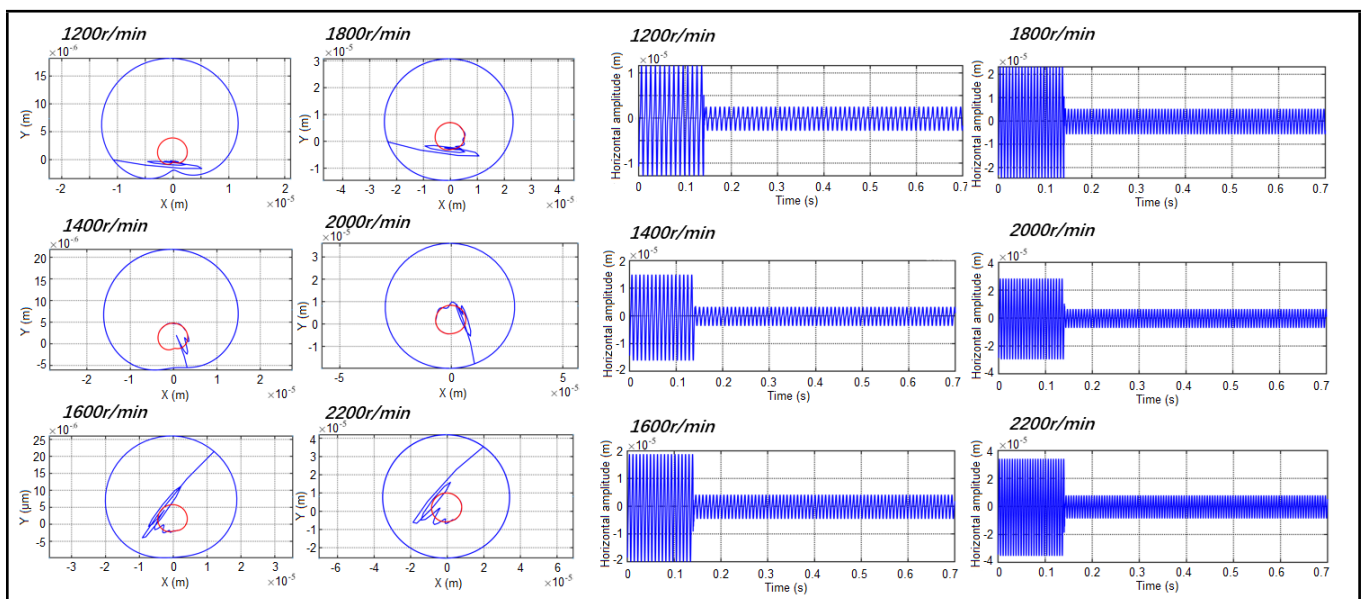


Figure 10. Diagram of axis trajectory and horizontal amplitude with fast differentiator control algorithm.

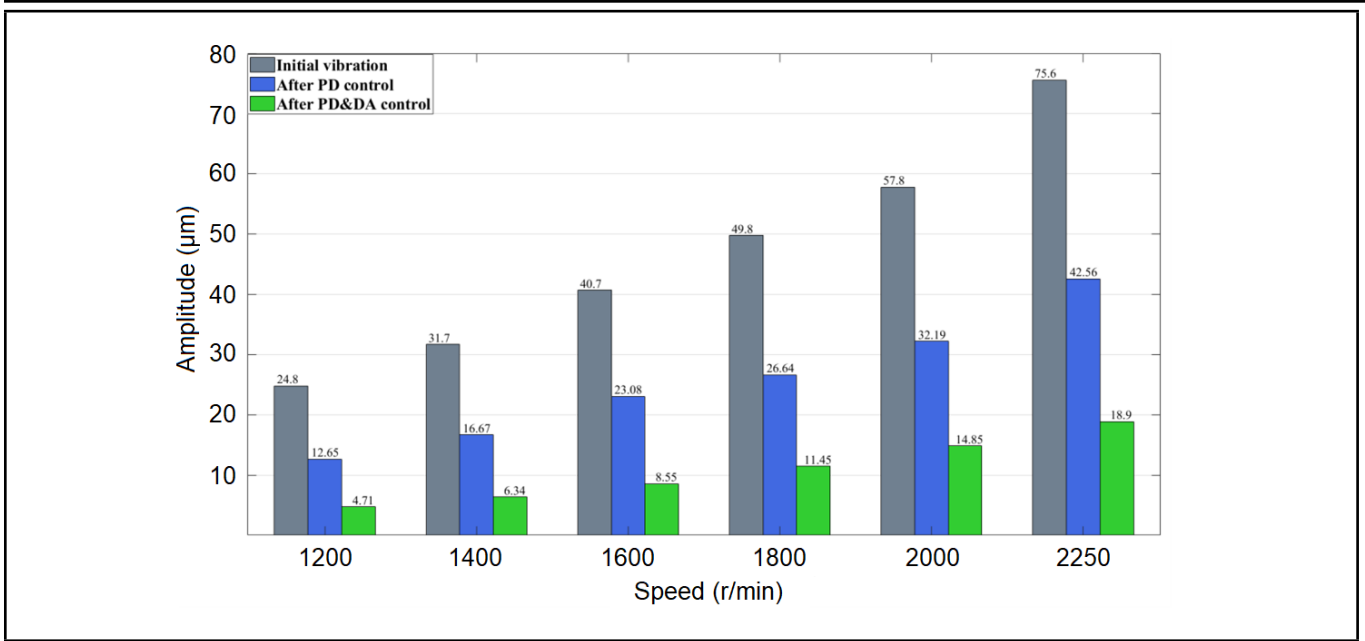


Figure 11. Comparison of rotor amplitude with and without control at multiple speed.

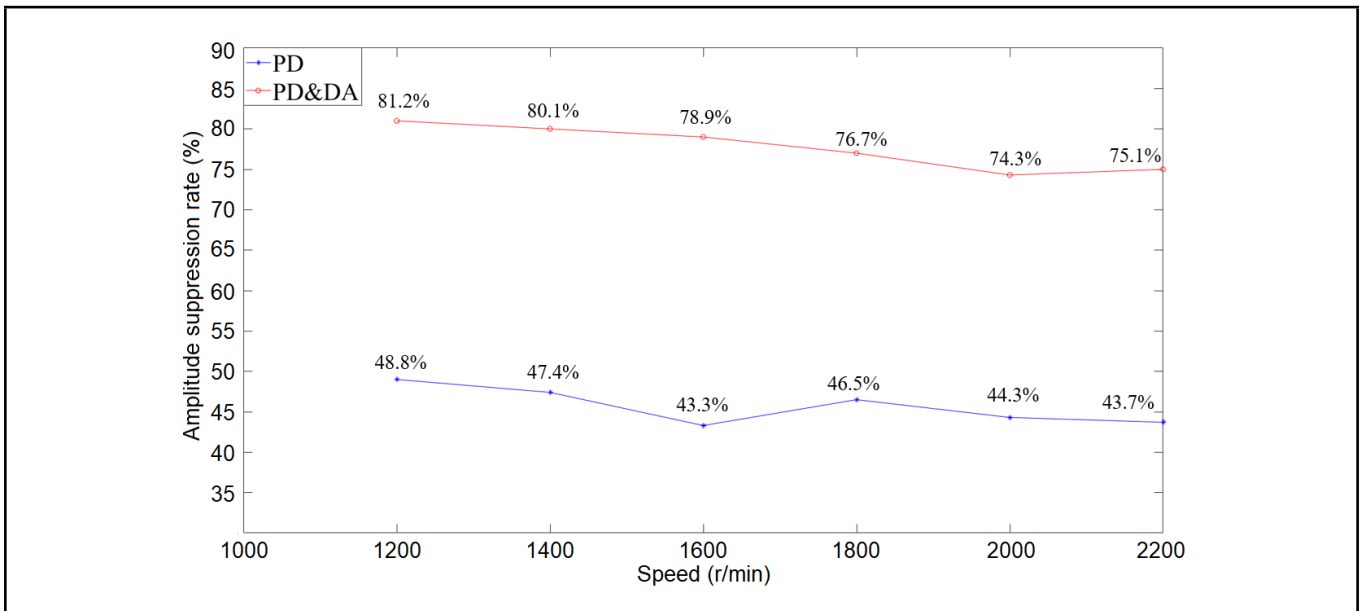


Figure 12. Rate of vibration suppression at multiple speed.

suppression effect is more stable. When the rotating speed of 1500 r/min is considered, the improved differential algorithm achieves 45.67% of amplitude rejection, while the PD control algorithm only achieves 28.73% (see Fig. 14). Therefore, the improvement of the stability of rotor vibration suppression effect after the algorithm improvement is verified.

The experiments of vibration suppression were conducted on the PD&DA algorithm and PD algorithm at various rotational speeds. The experimental results are depicted in Figs. 16 and 17. It is evident that as the rotational speed increases, the vibration amplitude produced by the system rises, along with the induced current in the coil. Figures 16 and 17 respectively display the trends in rotor amplitude and current signal over time for the PD control algorithm and the PD&DA control algorithm. The figures reveal that the control effectiveness and quality of the PD control algorithm deteriorate significantly with increasing rotational speed, whereas the PD&DA control

algorithm continues to demonstrate effective vibration control.

The vibration suppression rate of rotor in the *y*-direction at measuring point 1 at multiple speeds can be obtained from the vibration amplitude images in Figs. 16 and 17. Figure 18 illustrates the amplitude of rotor vibration in the *y*-direction at the measurement point of EA, comparing the results before and after control. The suppression rate formula is shown in Eq. (30). The results indicate that the PD&DA control achieves a suppression rate ranging from 33.4% to 50.5% when the proportional gain and differential gain *D* values are identical. Notably, this suppression effect is considerably superior to that of the conventional PD algorithm.

$$Q = \frac{V_1 - V_2}{V_1}; \tag{30}$$

where *Q* is the rotor vibration suppression rate, *V*₁ is the uncontrolled rotor vibration amplitude, *V*₂ is the controlled rotor

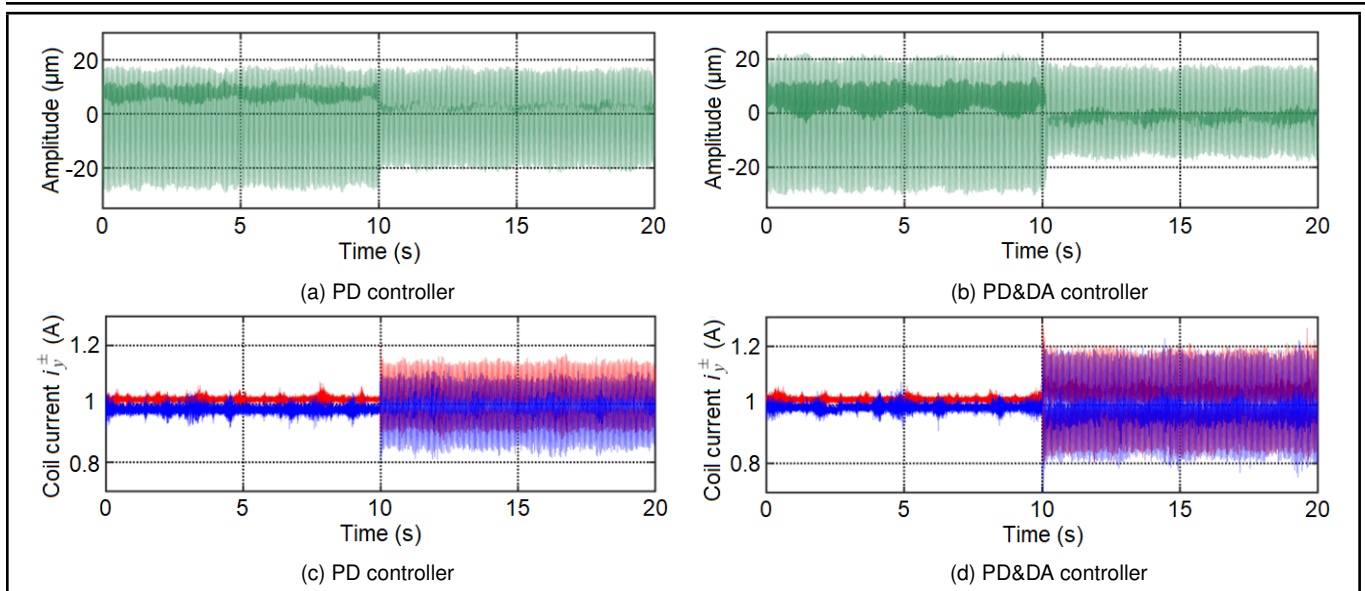


Figure 13. Amplitude of rotor vibration and Coil current of EA at 1350 r/min (y -direction).

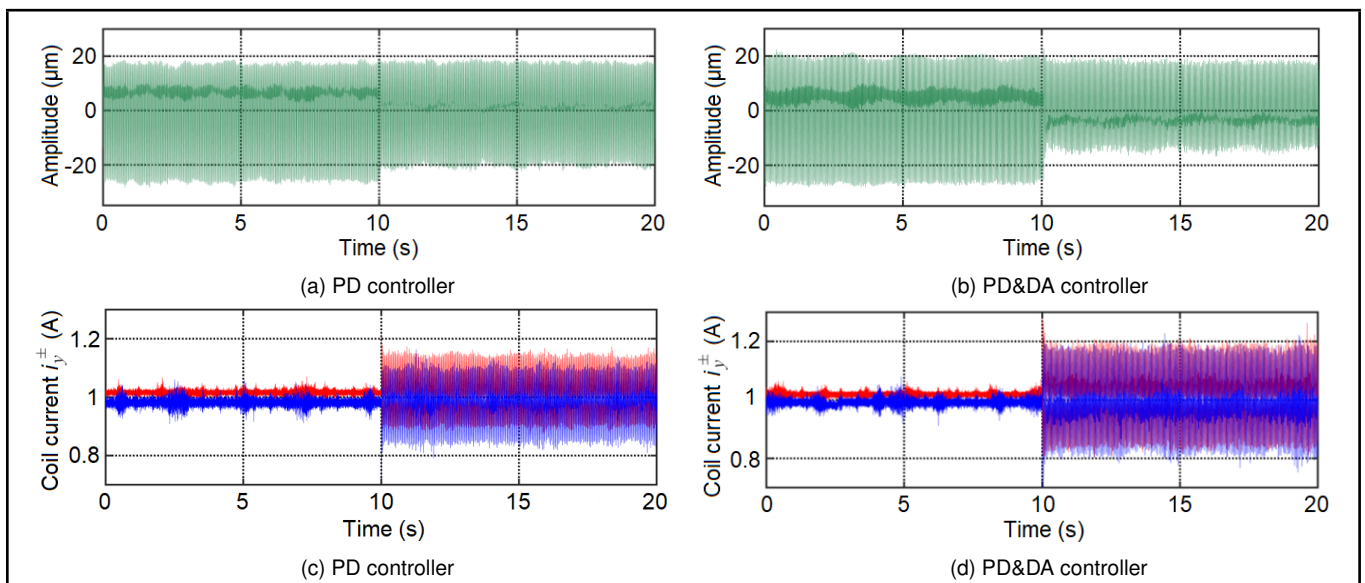


Figure 14. Amplitude of rotor vibration and Coil current of EA at 1500 r/min (y -direction).

vibration amplitude.

The effectiveness of experimental results from a frequency domain is examined. Figure 19 presents the frequency domain waterfall plot depicting the pre and post control at 1350 r/min and 1500 r/min, with the y -direction of measurement point #1. Figure 19 reveals a substantial reduction in both the first and second harmonic components, thereby substantiating the efficacy of the PD&DA algorithm in mitigating vibrations across multiple frequencies. Additionally, Fig. 19 provides clear evidence of the superior performance of the PD&DA algorithm in accurately identifying vibration signals and ensuring stable control. The PD algorithm exhibits limited accuracy in signal identification, and its stability falls short compared to the PD&DA algorithm in terms of control effectiveness.

6. CONCLUSIONS

This work used the coordinate system transformation method to decompose and synthesize multi frequency vector forces, and designed an active control algorithm for rotor multi

frequency vibration based on the improvement of differentiators.

1. An improved algorithm based on a differential device on rotor vibration suppression was proposed in the work. The results of simulation and experiments verified that the proposed method has a better suppression effect on rotor vibration generated by the imbalance and misalignment of the rotor than the convention PD control.
2. The algorithm optimized by the differentiator were a very good effect on signal extraction and rotor vibration control, and solved the problem that the conventional PD control algorithm was simple in structure, poor in robustness, and its vibration suppression rate reduced with the increase of rotating speed.
3. The differential optimization algorithm had better vibration suppression effect at low rotating speed, but whether the effect is attenuated at higher rotating speed needs to be verified by further research.

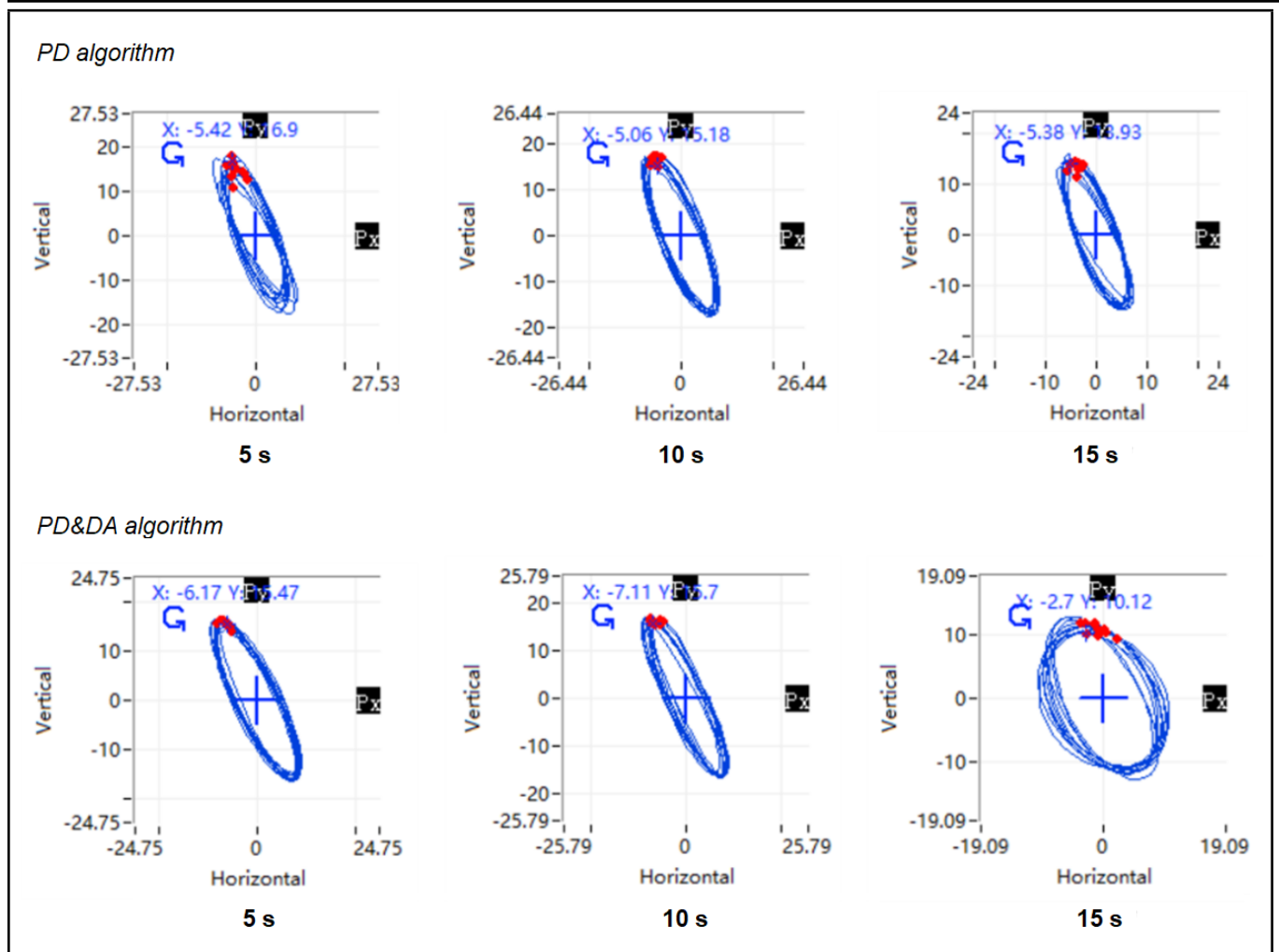


Figure 15. Experimental diagram of axial trajectory of front and rear rotors under control (1500 r/min).

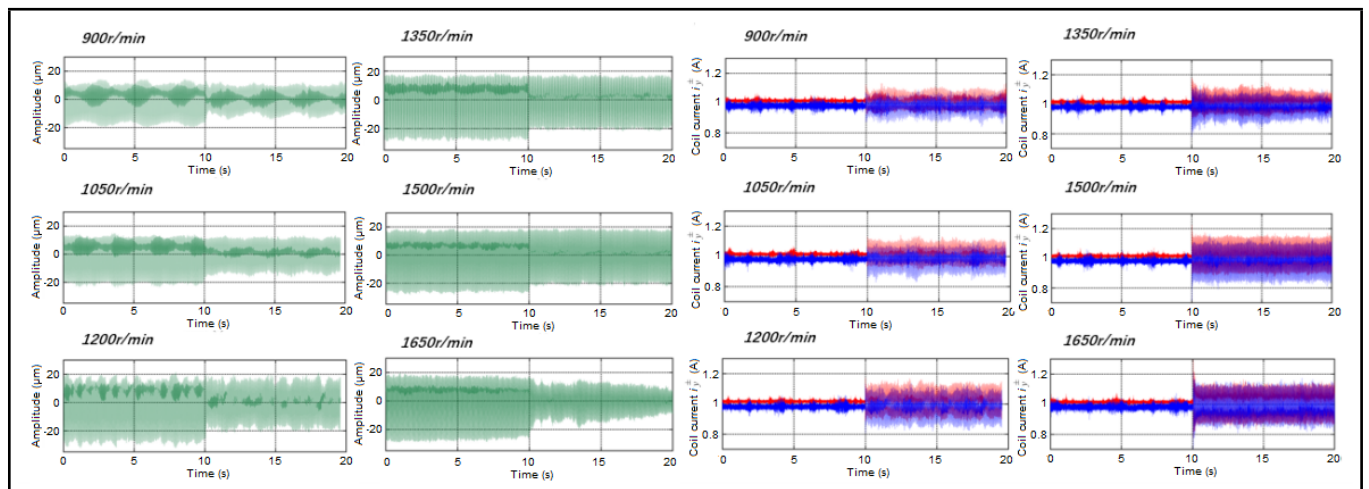


Figure 16. Comparison diagram of amplitude control effect and current variation at multiple speed (PD algorithm).

FUNDING

This work supported by Research Program supported by the National Natural Science Foundation of China (NSFC)(52375075, 51975037).

REFERENCES

- 1 Cao, Y., Li, Z., Dou, J., Jia, R., and Yao, H. An inerter non-linear energy sink for torsional vibration suppression of the rotor system, *Journal of Sound and Vibration*, **537**, 117184, (2022). <https://doi.org/10.1016/j.jsv.2022.117184>
- 2 Xu, H., Yang, Y., Ma, H., Luo, Z., Li, X., Han, Q., and Wen, B. Vibration characteristics of bearing-rotor systems with inner ring, *International Journal of Mechanical Sciences*, **230**, 107536, (2022). <https://doi.org/10.1016/j.ijmecsci.2022.107536>
- 3 Chweitzer, G. and Maslen, E. H. Theory, design and appli-

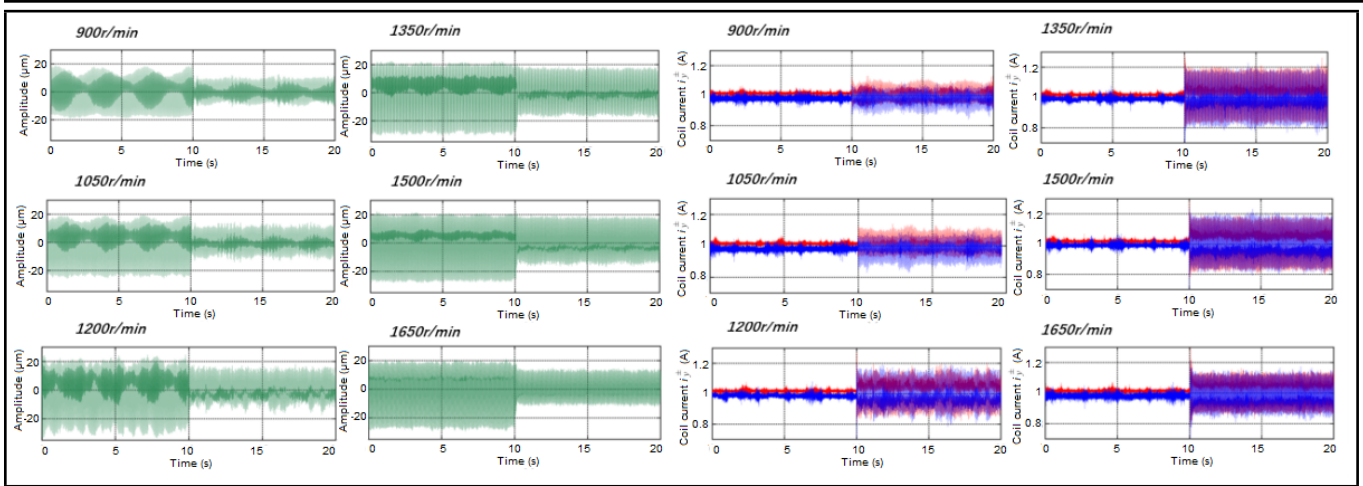


Figure 17. Comparison diagram of amplitude control effect and current variation at multiple speed (PD&DA algorithm).

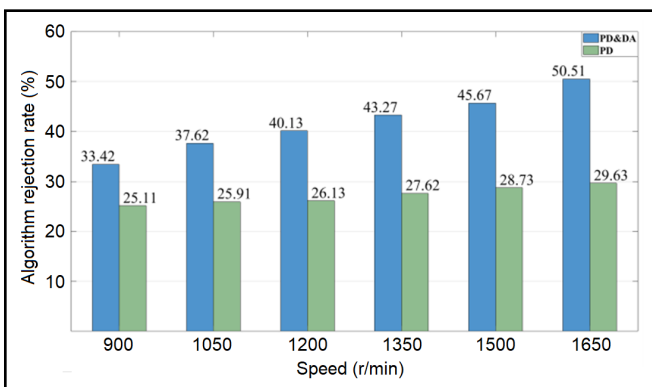


Figure 18. The suppression rate of rotor vibration in y -direction of the measurement point 1 at multi speeds.

cation to rotating machinery, *Magnetic Bearings*, 191–228, (2009). <https://doi.org/10.1007/978-3-642-00497-1>

- 4 Jianfei, Y., Jinji, G., Weimin, W. Multi-frequency vibration active suppression of rotor by self-optimizing electromagnetic force parameters, *Vibration and Shock*, **23** (5), 701–715, (2017). <https://doi.org/10.13465/j.cnki.jvs.2015.18.008>
- 5 Bleuler, H. A survey of magnetic levitation and magnetic bearing types, *JSME International Journal. Ser. 3, Vibration, Control Engineering, Engineering for Industry*, **35** (3), 335–342, (1992). <https://doi.org/10.1299/jsmec1988.35.335>
- 6 Bin, Z. and Changsheng, Z. Design of active electromagnetic bearing-rotor system controller (in Chinese), *Zhejiang University*, **50** (10), 1, (2016).
- 7 Kejian, J. and Changsheng, Z. Multi-objective weighted active vibration control of electromagnetic bearing-flexible rotor system (in Chinese), *Journal of Zhejiang University*, **50** (10), 133, (2016).
- 8 Zhongbo, W., Chuan, M., and Changsheng, Z. Current compensation control of multi-frequency vibration of electromagnetic bearing high-speed motor rotor (in Chinese), *Chinese Journal of Electrical Engineering*, **38** (1), 10, (2018). <https://doi.org/10.13334/j.0258-8013.pcsee.171586>
- 9 Guo, Y., Yao, J., and Li, Y. Dynamic balancing of multispeed multidisk rotor, *Journal of Vibration Engineering & Technologies*, **37**, 2263–2274, (2023). <https://doi.org/10.1007/s12206-023-0403-z>
- 10 Deng, S., Cheng, X., Wu, H., and Hu, Y. Multi-objective optimization configuration of redundant electromagnetic actuators in fault-tolerant control of active magnetic bearing system, *ISA Transactions*, **140**, 293–308, (2023). <https://doi.org/10.1016/j.isatra.2023.06.015>
- 11 Jinfei, Y., Jinji, G., and Weimin, W. Multi-frequency rotor vibration suppressing through self-optimizing control of electromagnetic force, *Journal of Vibration and Control*, **23** (5), 701–715, (2017). <https://doi.org/10.1177/10775463155586301>
- 12 Jianfei, Y., Liang, L., and Weimin, W. Research on multi-frequency rotor vibration suppression for quick optimization of electromagnetic force parameters, *Vibration, Testing and Diagnosis*, **38** (4), 738–743, (2018). <https://doi.org/10.16450/j.cnki.issn.1004-6801.2018.04.013>
- 13 Niu, W., Zou, C., Li, B., and Wang, W. Adaptive vibration suppression of time-varying structures with enhanced FxLMS algorithm, *Mechanical Systems and Signal Processing*, **118**, 93–107, (2019). <https://doi.org/10.1016/j.ymsp.2018.08.009>
- 14 Zhou, D. F., Li, J., and Hansen, C. H. Application of least mean square algorithm to suppression of maglev track-induced self-excited vibration, *Journal of Sound and Vibration*, **330**, 5791–5811, (2011). <https://doi.org/10.1016/j.jsv.2011.07.021>
- 15 Lin, J. and Zheng, Y. B. Vibration suppression control of smart piezoelectric rotating truss structure by parallel neuro-fuzzy control with genetic algorithm tuning, *Journal of Sound and Vibration*, **331**, 3677–3694, (2012). <https://doi.org/10.1016/j.jsv.2012.04.001>
- 16 Saldanha, A., Silm, H., Michiels, W., and Vyhlídal, T. An optimization-based algorithm for simultaneous shaping of poles and zeros for non-collocated vibration

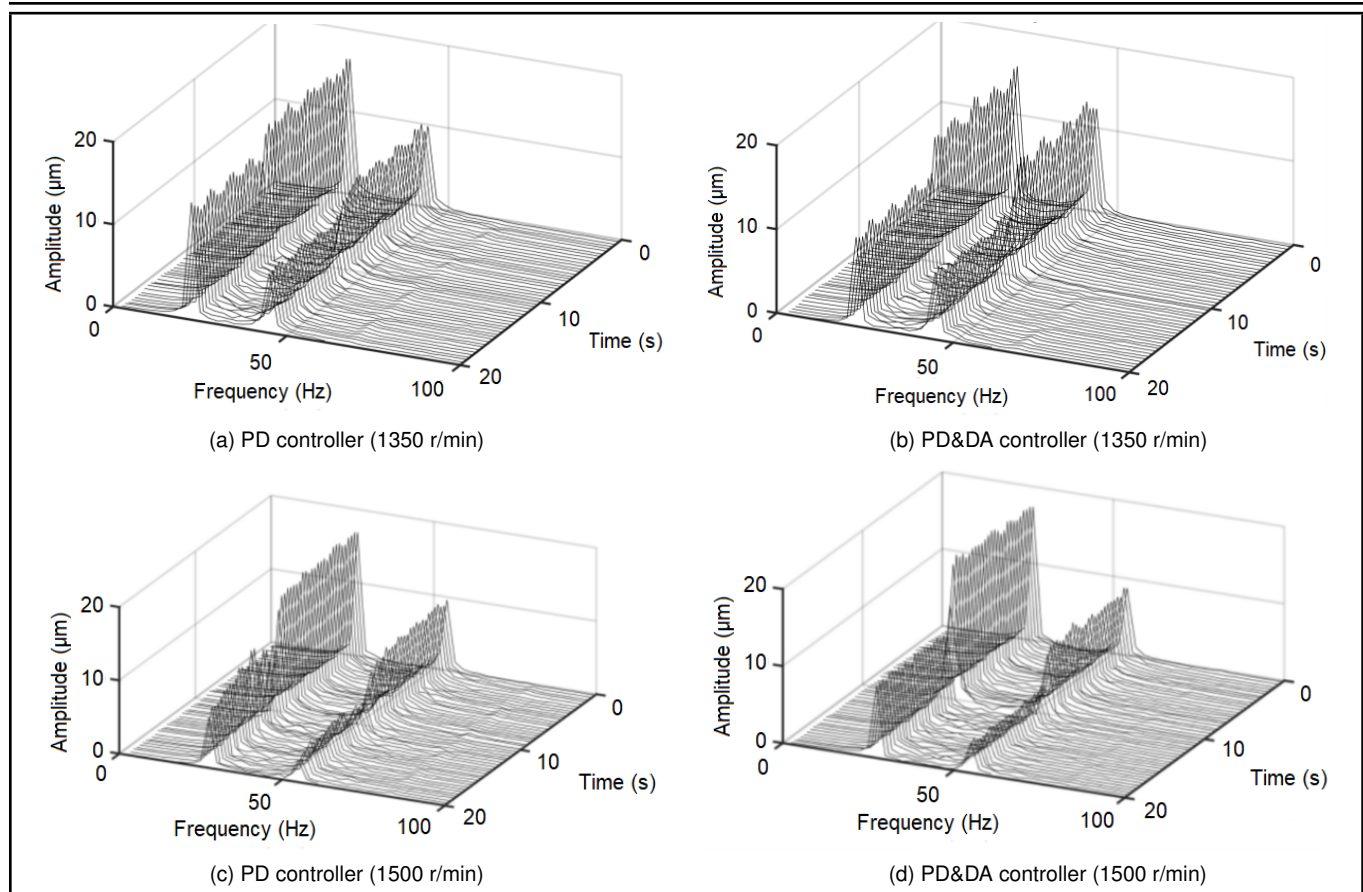


Figure 19. Slope Chart of measuring point #1 in the y -direction at the speed of 1350 r/min and 1500 r/min.

- suppression, *IFAC-PapersOnLine*, **55**, 394–399, (2022). <https://doi.org/10.1016/j.ifacol.2022.09.056>
- ¹⁷ Zheng, S. Q. and Feng, R. Feedforward compensation control of rotor imbalance for high-speed magnetically suspended centrifugal compressors using a novel adaptive notch filter, *Journal of Sound and Vibration*, **366**, 1–14, (2016). <https://doi.org/10.1016/j.jsv.2015.12.029>
- ¹⁸ Yao, J. F., Dai, J. B., and Liu, L. Unbalanced vibration response reduction of rotor using active magnetic actuator based on PD control, *International Journal of Acoustic and Vibration*, **24** (2), 327–333, (2019). <https://doi.org/10.20855/ijav.2019.24.21517>
- ¹⁹ Bao, Y. F., Yao, J. F., and Scarpa, F. A modified iterative learning control approach for the active suppression of rotor vibration induced by coupled unbalance and misalignment, *Chinese Journal of Mechanical Engineering*, **37** (12), 2–12, (2024). <https://doi.org/10.1186/s10033-024-00994-x>
- ²⁰ Gao, X., Bao, Y., Zhang, Z., and Yao, J. Active suppression of multi-frequency vibration of rotor based on adaptive immersion & invariant theory, *IFTToMM 2023: Proceedings of the 11th IFTToMM International Conference on Rotordynamics*, 54–70, (2023). https://doi.org/10.1007/978-3-031-40455-9_6
- ²¹ Stančić, G., Krstić, I., Kostić, I., and Petrović, M. Design of IIR full-band differentiators with improved nearly linear phase, *Digital Signal Processing*, **144**, 104276, (2024). <https://doi.org/10.1016/j.dsp.2023.104276>
- ²² Zhang, H., Liang, Y., and Cheng, H. Convergence analysis on a tracking differentiator used in active disturbance rejection control, *ISA Transactions*, **141**, 392–400, (2023). <https://doi.org/10.1016/j.isatra.2023.07.005>
- ²³ Seeber, R. Worst-case error bounds for the super-twisting differentiator in presence of measurement noise, *Automatica*, **152**, 110983, (2023). <https://doi.org/10.1016/j.automatica.2023.110983>
- ²⁴ Pei, S. C. and Shyu, J. J. Design of FIR Hilbert transformers and differentiators by eigenfilter, *IEEE Transactions on Circuits and Systems*, **35**, 505–511, (1988). <https://doi.org/10.1109/31.14474>
- ²⁵ B. Kumar, B. and Roy, S. C. D. Design of digital differentiators for low frequencies, *Proceedings of the IEEE*, **76**, 287–289, (1988). <https://doi.org/10.1109/5.4408>
- ²⁶ Xinhua, W. and Jinkun, L. Differentiator design and application—Signal filtering and differentiation, *Beijing: Electronic Industry Press*, **4**, 1, (2010).
- ²⁷ Xinhua, W., Qiang, C., and Zhuzhi, Y. All-round fast non-linear tracking-differential device, *Control Theory and Application*, **20** (6), 875–878, (2003).
- ²⁸ Yi'e, Z. *Rotor Dynamics* (in Chinese), Beijing, Tsinghua University Press, 207–210, (1987).
- ²⁹ Khalil, H. Robust servomechanism output feedback controller for feedback linearizable systems, *Automatica*, **30**, 1587–1599, (1994). [https://doi.org/10.1016/0005-1098\(94\)90098-1](https://doi.org/10.1016/0005-1098(94)90098-1)